2014

Eruptive timing and 200 year episodicity at 92°W on the hot spot-influenced Galapagos Spreading Center derived from geomagnetic paleointensity

Julie A. Bowles
University of Wisconsin-Milwaukee, bowlesj@uwm.edu

Alice Colman
University of Hawaii, Manoa

J. Timothy McClinton
University of South Carolina - Columbia

John Sinton
University of Hawaii, Manoa

Scott M. White
University of South Carolina - Columbia

See next page for additional authors

Authors
Julie A. Bowles, Alice Colman, J. Timothy McClinton, John Sinton, Scott M. White, and Kenneth H. Rubin

AGU PUBLICATIONS

Geochemistry, Geophysics, Geosystems

RESEARCH ARTICLE
10.1002/2014GC005315

Key Points:
- Eruptive timing is episodic for largest flows with a ~200 year repose interval
- Average recurrence interval maximum is 25–50 years
- Paleointensity dating in high-Fe flows requires large sample numbers

Supporting Information:
- Supplementary Table 1
- Supplementary Figure 1
- ReadMe

Correspondence to:
J. A. Bowles,
bowlesj@uwm.edu

Citation:
Bowles, J. A., A. Colman, J. T. McClinton, J. M. Sinton, S. M. White, and K. H. Rubin (2014), Eruptive timing and 200 year episodicity at 92°W on the hot spot-influenced Galapagos Spreading Center derived from geomagnetic paleointensity, *Geochem. Geophys. Geosyst.*, *15*, doi:10.1002/2014GC005315.

Received 21 FEB 2014
Accepted 8 MAY 2014
Accepted article online 12 MAY 2014

Eruptive timing and 200 year episodicity at 92°W on the hot spot-influenced Galapagos Spreading Center derived from geomagnetic paleointensity

Julie A. Bowles[1], Alice Colman[2], J. Timothy McClinton[3], John M. Sinton[2], Scott M. White[3], and Kenneth H. Rubin[2]

[1]Department of Geosciences, University of Wisconsin-Milwaukee, Milwaukee, Wisconsin, USA, [2]Department of Geology and Geophysics, University of Hawaii at Manoa, Honolulu, Hawaii, USA, [3]Department of Earth and Ocean Sciences, University of South Carolina, Columbia, South Carolina, USA

Abstract Eruptive timing in mid-ocean ridge systems is relatively poorly constrained, despite being an important variable in our understanding of many mid-ocean ridge processes, including volcanic construction; magma recharge, flux, and storage; and the stability of hydrothermal systems and biological communities. Only a handful of absolute eruption chronologies exist, yet they are essential in understanding how eruptive timing varies with important controlling variables. To construct an eruptive history at one location on the Galapagos Spreading Center, we present age determinations derived from geomagnetic paleointensity. To aid interpretation of the paleointensity data, we also present results from on-bottom magnetic anomaly measurements and forward modeling of topographic-induced magnetic anomalies. Anomalies may lead to a 1–2 μT bias in flow-mean paleointensities, which does not significantly affect the overall interpretation. Paleointensity results for the three youngest sampled units are indistinguishable, consistent with the flows being emplaced in relatively rapid succession. Comparisons with models of geomagnetic field behavior suggest these flows were erupted sometime in the past 100–200 years. The fourth sampled unit has a significantly higher paleointensity, consistent with an age of roughly 400 years. The possible bias in paleointensity data allows for ages as young as ~50 years for the youngest three flows and 200–400 years for the oldest flow. This age distribution demonstrates an episodicity in the emplacement of the largest flows at this location, with a 200–300 year period of relative quiescence between emplacement of the oldest unit and the three youngest units.

1. Introduction

Along mid-ocean ridges, eruption frequency, size, and morphology have been observed to be inversely correlated with spreading rate; smaller, more frequent eruptions comprised of a higher proportion of sheet flows are often found at higher spreading rates [*Perfit and Chadwick*, 1998; *Sinton et al.*, 2002]. While in most cases, magma supply varies with spreading rate over long time scales, over shorter time scales (hundreds to thousands of years), local magma supply may vary dramatically, and any individual ridge segment may oscillate from extension under primarily magmatic to primarily tectonic conditions [*Kappel and Ryan*, 1986; *Perfit and Chadwick*, 1998; *Sinton et al.*, 2002; *Fornari et al.*, 1998; *Cormier et al.*, 2003; *Ito and Behn*, 2008]. The same volumetric magma supply at fast versus slow spreading may also result in vastly different seafloor morphology, resulting from differing eruptive style, size, and timing.

Eruption frequency, in particular, is relatively poorly constrained, despite being an important variable in our understanding of volcanic construction; magma recharge, flux, and storage; and the stability of hydrothermal systems and biological communities [e.g., *Fornari et al.*, 2012; *Rubin et al.*, 2012]. Excepting Iceland, fewer than 12 historical eruptions have been documented on the mid-ocean ridge system (see *Rubin et al.* [2012] for overview), and in only three instances have repeat eruptions occurred at the same location. By contrast, in Iceland, where the Mid-Atlantic Ridge rises above sea level, >1000 years of historical observations show that there, eruptions are episodic in nature, with several eruptions clustering together in a short time separated by longer periods of tens to hundreds of years with no volcanic activity [*Gudmundsson*, 2000; *Sinton et al.*, 2005]. Recent data from Axial seamount (constrained by ^{14}C dates) suggest a slightly different pattern: at least two phases of frequent eruptions lasting ~250–350 years separated by a relatively

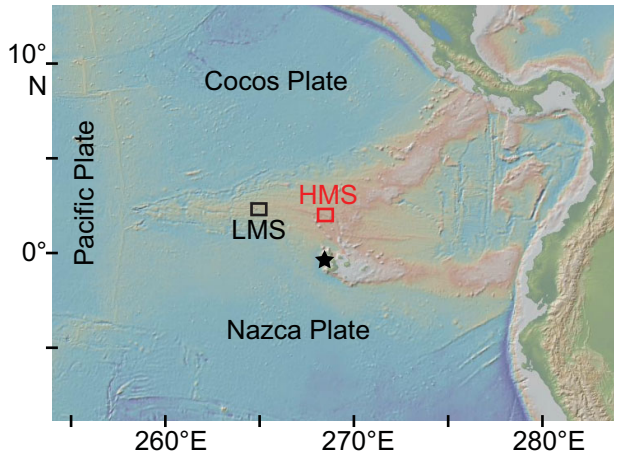

Figure 1. Overview map of study area. Low-magma-supply (LMS) and high-magma-supply (HMS) study areas shown by boxes. HMS enlarged in Figure 2. Approximate location of Galapagos hot spot shown by star. Basemap generated with GeoMapApp (www.geomapapp.org) [*Ryan et al*., 2009].

quiescent phase of approximately equal duration [*Clague et al*., 2013]. It may be argued that hot spot-influenced Iceland and Axial seamount do not represent "normal" mid-ocean ridge eruption conditions, but some geomagnetic paleointensity and radiometric age data from the southern [*Bergmanis et al*., 2007] and northern [*Bowles et al*., 2006] East Pacific Rise also are consistent with a model of episodic volcanic activity. Determining similarities or differences between different mid-ocean ridge environments, however, requires significantly more data than currently exist.

The difficulties in determining mid-ocean ridge eruption frequency are linked to challenges in absolute dating of young flows (<10,000 years) where the shortest eruptive recurrence intervals are estimated to be as frequent as years to decades, and most radiometric systems have limited resolution (>1 ka). In cases of very young flows (<100 years), short-lived radiometric methods are increasingly being used [e.g., *Bergmanis et al*., 2007; *Rubin et al*., 1994, 2005; *Sims et al*., 2008], and radiocarbon dating of overlying foraminifera-bearing sediments has recently been used to provide lower limits on eruptive ages [*Clague et al*., 2013; *Dreyer et al*., 2013]. Superposition, variations in sediment cover, or fault density give information on relative timing, but it is not always easy to find onlapping relationships, and apparent sediment cover can vary with flow morphology and bottom currents.

In part to answer questions linking eruptive timing to magma supply, two contrasting sites were selected on the GSC, a relatively low-magma-supply (LMS) area at 95°W and a relatively high-magma-supply (HMS) area closer to the hot spot at 92°W (Figure 1). The two study areas were mapped using high-resolution swath bathymetry, submersible observations, and camera tow photography [*Colman et al*., 2012; *McClinton et al*., 2013]. Individual eruptive units (or flow fields) have been identified on the basis of these data, as well as sample geochemistry [*Colman et al*., 2012]. Here an eruptive unit may comprise more than one eruptive event, but the events are closely associated in both space and time and display common geochemical fingerprints. Where possible, a relative eruption sequence was determined from flow superposition.

In order to construct a more detailed eruptive history and to make broader interpretations regarding eruptive frequency and processes, it is necessary to place relative ages in an absolute time frame. To do this, we use geomagnetic paleointensity that is recorded by volcanic glass on eruption. Variations in paleointensity have been successfully used to place age constraints on young submarine flows [*Carlut and Kent*, 2000; *Carlut et al*., 2004; *Bowles et al*., 2005, 2006, 2011; *Searle et al*., 2010]. This technique relies upon independent knowledge of secular variations in the core-derived magnetic field, and one of the sources of error is a contribution to the magnetic field from local magnetic topography. The size of these local magnetic anomalies is related to seafloor gradients, geographic orientation of topographic features, and magnetization intensity of preexisting flows. Compared to earlier efforts on the north-south trending East Pacific Rise [*Carlut and Kent*, 2000; *Carlut et al*., 2004; *Bowles et al*., 2005, 2006] and Mid-Atlantic Ridge [*Searle et al*., 2010], it is expected that local anomalies will be greater on the GSC, where the east-west trending spreading center has an unfavorable geometry with respect to the northerly magnetic vectors, and because the relatively Fe-rich basalts are more magnetic on this part of the ridge [e.g., *Anderson et al*., 1975; *Vogt and De Boer*, 1976]. However, with sufficient geographic sampling within a given flow field, it has been suggested that such topographic-induced variation could be averaged out or minimized [*Valet and Soler*, 1999; *Tanguy and Le Goff*, 2004].

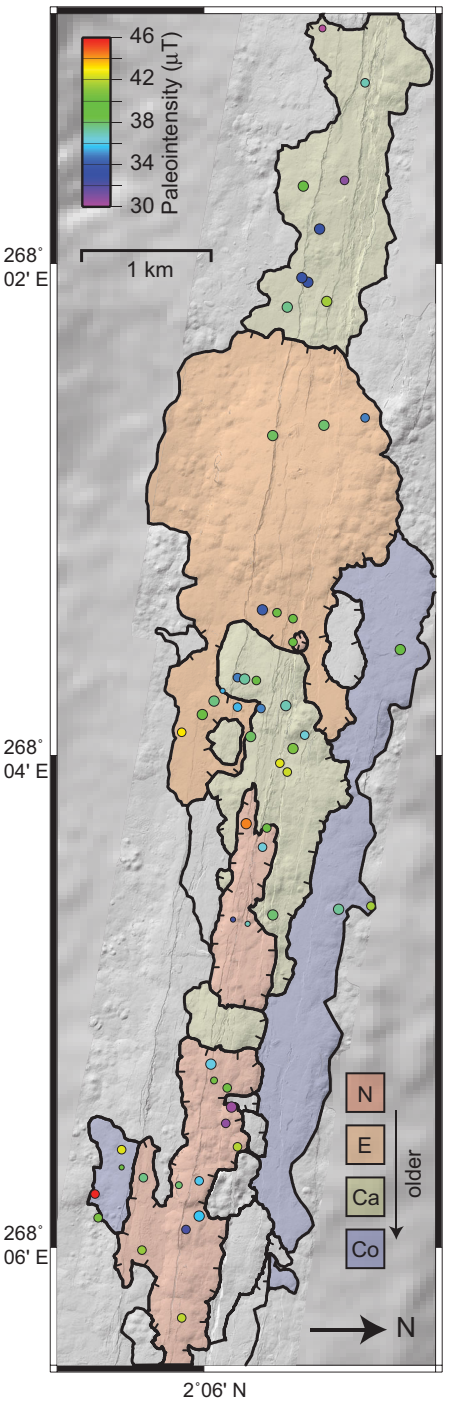

Figure 2. Mapped flow fields at the high-magma-supply study area. Shaded flows are described in the text: N = Ninos; E = Empanada; Ca = Calor; Co = Cobija. Relative ages determined on the basis of submersible observations and camera-tow images are N < E < Ca < Co, and tick marks indicate younger flow. Sample-level paleointensity results are shown by colored symbols. Over the time scales that these flows were emplaced, geomagnetic paleointensity should be mostly decreasing to the present-day value of 31.5 μT. Symbol size correlates with standard error such that larger symbols have smaller standard errors.

Here we apply the paleointensity dating technique in an area characterized by relatively large near-bottom anomalies. We present results of paleointensity experiments on four mapped lava flow fields from the HMS study area. Results are interpreted in the context of both measured and modeled near-bottom magnetic anomalies in order to derive age and eruptive recurrence interval estimates.

2. Geologic Setting

We selected the eastern, HMS study area for the paleointensity test case. Centered at ~91°55′W near the center of a third-order spreading segment, increased magma supply from the hot spot results in an axial rise at this study area [*Sinton et al.*, 2003]. Minimal sediment cover on the on-axis flows suggests that they are <500 years old. Over this time period, geomagnetic field intensity has been predominantly decreasing, and a lower paleointensity can be interpreted as a younger probable age. Additionally, a lower proportion of high-relief pillow lava mounds [*Colman et al.*, 2012; *McClinton et al.*, 2013] suggests local topographically produced anomalies will be lower. Within the study area, we selected the four largest mapped flow fields in order to take advantage of the high number of samples per flow unit.

The sampled flow units are shown in Figure 2 and are described in detail in *Colman et al.* [2012]. The Cobija eruptive unit has the thickest sediment cover, extends farthest off axis, and is comprised of relatively low-relief pillow, lobate, and sheet flows. This is likely the oldest mapped unit shown in Figure 2. The Calor flow field is centered along the rise axis, and its exposure along ~8 km of ridge axis is interrupted by a large, flat-topped seamount. Calor consists of a hummocky ridge, and several hydrothermal chimneys (some active in April 2010) are present near its eastern boundary

with the Ninos pillow ridge (see below). The seamount, Empanada, is ~100 m tall and ~2 km in diameter. The summit plateau consists largely of lobate flows, the flanks of pillows, and a series of sheet flows to the east of the seamount also are correlated with this eruptive unit. The relative ages of Calor and Empanada are not entirely clear, but because Empanada is less faulted and bisects the Calor ridge, we tentatively conclude that it is younger. To the east, the Ninos eruptive unit consists of a discontinuous pillow ridge, also extending along axis. The ridge is up to 40 m tall and is interpreted to be the youngest mapped flow field in the HMS site. It is cut by relatively few faults; active hydrothermal venting was observed in the western part of the flow field; and extinct chimneys, with largely inactive clam and mussel shell beds, were found throughout.

3. Methods

3.1. Paleomagnetic Measurements

Rock samples were collected by *DSV* Alvin submersible, and 8–20 samples from each eruptive unit were selected for paleointensity analyses. Glass from sample margins was used because the fine grain size of the magnetic particles best satisfies the conditions of remanence reciprocity and additivity required for double-heating paleointensity experiments. The 303 unoriented glass specimens representing 64 samples were prepared for paleointensity analysis by soaking in a dilute HCl solution and then immobilizing in small glass tubes. Thellier-type [*Thellier and Thellier*, 1959] paleointensity experiments were carried out in an applied field of 40 μT using the IZZI (In field-Zero field, Zero field-In field) protocol [*Tauxe and Staudigel*, 2004], which alternates the order in which the in-field and zero-field treatments are applied. Specimens were heated in 50°C steps between 100 and 200°C and then in 25°C steps up to 550°C. Partial thermal remanent magnetism (pTRM) checks [*Coe*, 1967] were carried out every other temperature step as a check against sample alteration. Experiments were conducted in the shielded room at the Institute for Rock Magnetism at the University of Minnesota. Specimens were heated in air in an ASC TD4-SC thermal demagnetizer with field coil and were measured on a 2G superconducting rock magnetometer with DC SQUID sensors.

Data were processed as in *Bowles et al*. [2005], where a bootstrap resampling of all possible slopes on the natural remanent magnetism (NRM) versus pTRM plot is done to avoid subjectivity in picking the slope. To be included in the bootstrap resampling, an individual slope must contain at least four points, represent >50% of the NRM ($f > 0.5$) [*Coe et al*., 1978], and have a maximum difference ratio (DRAT) of <10. The DRAT [*Selkin and Tauxe*, 2000] is a check against thermochemical alteration and is defined as the difference between two repeat in-field steps, normalized by the length of the NRM-pTRM segment. Data passed to the bootstrap start at T_{low} where any viscous component or overprint is removed and end at T_{high}, when <~5% of the NRM remains or when NRM ceases to be removed. The one exception to this rule is a subset of specimens run together in a single boat. For these specimens (to various degrees) at temperatures between ~200 and 300°C, pTRM is gained, but no NRM is removed. There is no obvious cause for this problem; temperatures recorded during the heating were all normal. For these samples, we select only the temperature steps above the affected interval for passing to the bootstrap program. Resulting paleointensity values derived from these specimens are not significantly different from sister specimens without the problem, so we chose to include them in the final analyses. These specimens are flagged in supporting information Table S1.

Magnetic hysteresis measurements were carried out on a subset of sister specimens (not subjected to paleointensity experiments) in order to characterize magnetic grain size as an aid in data interpretation. Magnetization was measured as a function of applied field up to 1T on a Princeton Measurements vibrating sample magnetometer at the Institute for Rock Magnetism. Data were processed as in *Jackson and Solheid* [2010], and because of the high paramagnetic/ferromagnetic ratio of most specimens, loops were fit with a set of hyperbolic basis functions before calculating loop parameters.

3.2. Magnetic Anomaly Measurements and Modeling

To assess the magnitude of the topographically induced near-bottom anomalies, three-axis magnetometer data were collected on most dives. The IFG fluxgate magnetometer has a stated accuracy of 1000 nT, resolution of 0.1 nT, and was mounted on *Alvin*'s sail (~3 m above the vehicle base). A correction for the vehicle-

induced field was carried out by rotating the vehicle about a vertical axis several times during descent and ascent [*Tivey et al*., 1993]. The resulting field variation with vehicle heading was then subtracted from the raw data, and the International Geomagnetic Reference Field (IGRF) was subtracted to give the final anomaly data. In assessing the magnitude of on-bottom anomalies, we used data only from periods when the vehicle was taking rock samples. In these instances, the vehicle was typically sitting on the seafloor with minimal movement, and the magnetometer was thus at a constant height above the bottom. The resulting on-bottom anomalies of up to approximately ±14,000 nT were considerably greater than the typical heading correction of less than ±1000 nT.

To supplement these measured on-bottom anomalies, which were restricted to sampling sites, we generated forward models of magnetic anomalies produced by typical seafloor terrain in the study area. We selected one area dominated by small, hummocky mounds from the LMS study region [*Colman et al*., 2012] and one area from the HMS study region dominated by faults and fractures trending approximately west-northwest to east-southeast. High-resolution bathymetry data are described in *McClinton et al*. [2013]. The two subsets of bathymetry data were regridded at 2 m resolution, and a three-dimensional forward model was produced using algorithms based on *Blakely* [1996]. The model was evaluated at a constant height of 10 m above the bathymetry, and the ambient magnetic field used was the IGRF value of 5° declination and 23° inclination. The source layer was assumed to be 300 m thick with a uniform magnetization in the direction of the time-averaged field (0° declination and 4.5° inclination). Magnetization intensity was set to 35 Am^{-1} based on measurements from a limited number of crystalline basalt samples and assuming a density of 2950 kg m^{-3}. This magnetization value is within the range of 9–85 Am^{-1} reported from dredge samples [*Anderson et al*., 1975; *Vogt and De Boer*, 1976] and is in approximate agreement with NRM values reported by *Gee and Kent* [1998] for basalts with similar Fe content.

4. Results

4.1. Rock Magnetic and Paleointensity Results

Hysteresis data (supporting information Figure S1) demonstrate that the magnetic carrier in the samples is similar to that in other submarine basaltic glass (SBG) [*Bowles et al*., 2006, 2011], with magnetic grain sizes ranging between superparamagnetic and single domain. Unblocking temperatures are typically distributed between 100°C and 500°C, again consistent with other SBG samples and with low-Ti titanomagnetite as the dominant carrier.

Paleointensity data are typically of high technical quality, and representative data are shown in Figure 3. Sample-level paleointensity averages are summarized in Table 1, and Figures 2 and 4 demonstrate spatial variability in paleointensity. Specimen-level results are given in supporting information Table S1. Flow unit means and standard errors (Table 2 and Figure 4) were calculated via bootstrap resampling in order to propagate sample-level uncertainty to the flow-mean level. The mean values of the three youngest flows cannot be statistically distinguished at the 1 standard error level, while that for the oldest flow (Cobija) is significantly different. Likewise, a *t* test (which does not include sample-level uncertainty) indicates that a common mean for the three younger flows cannot be rejected at the 95% confidence level, while that of the older Cobija flow can.

4.2. Magnetic Anomaly Measurements and Modeling Results

In the HMS area alone, measured on-bottom anomalies range from −9.6 to 14.8 μT (Figure 5a), with near-zero mean (−0.2 μT) and median (−0.2 μT). When combined with measurements from the LMS area (Figure 5b), the mean and median are slightly more negative at −0.4 and −0.6 μT, respectively. The distribution skews slightly positive, with skewness = 0.6 for HMS alone (or 0.5 for the combined distribution). We note that these anomalies are much greater than the ±1.5 μT observed by *Tanguy and Le Goff* [2004] on Mt. Etna at ∼0.3 m above ground level or the ±5 μT observed by *Valet and Soler* [1999] at 0.65 and 1.5 m above ground level in the Canary Islands.

Results of the three-dimensional modeling produce near-bottom total field anomalies that are consistent with the observed anomalies. At 10 m above bottom, anomalies produced by the hummocky terrain range from −11.4 to 39.2 μT (Figures 6a and 6b), and by the faulted terrain from −11.6 to 28.5 μT (Figures

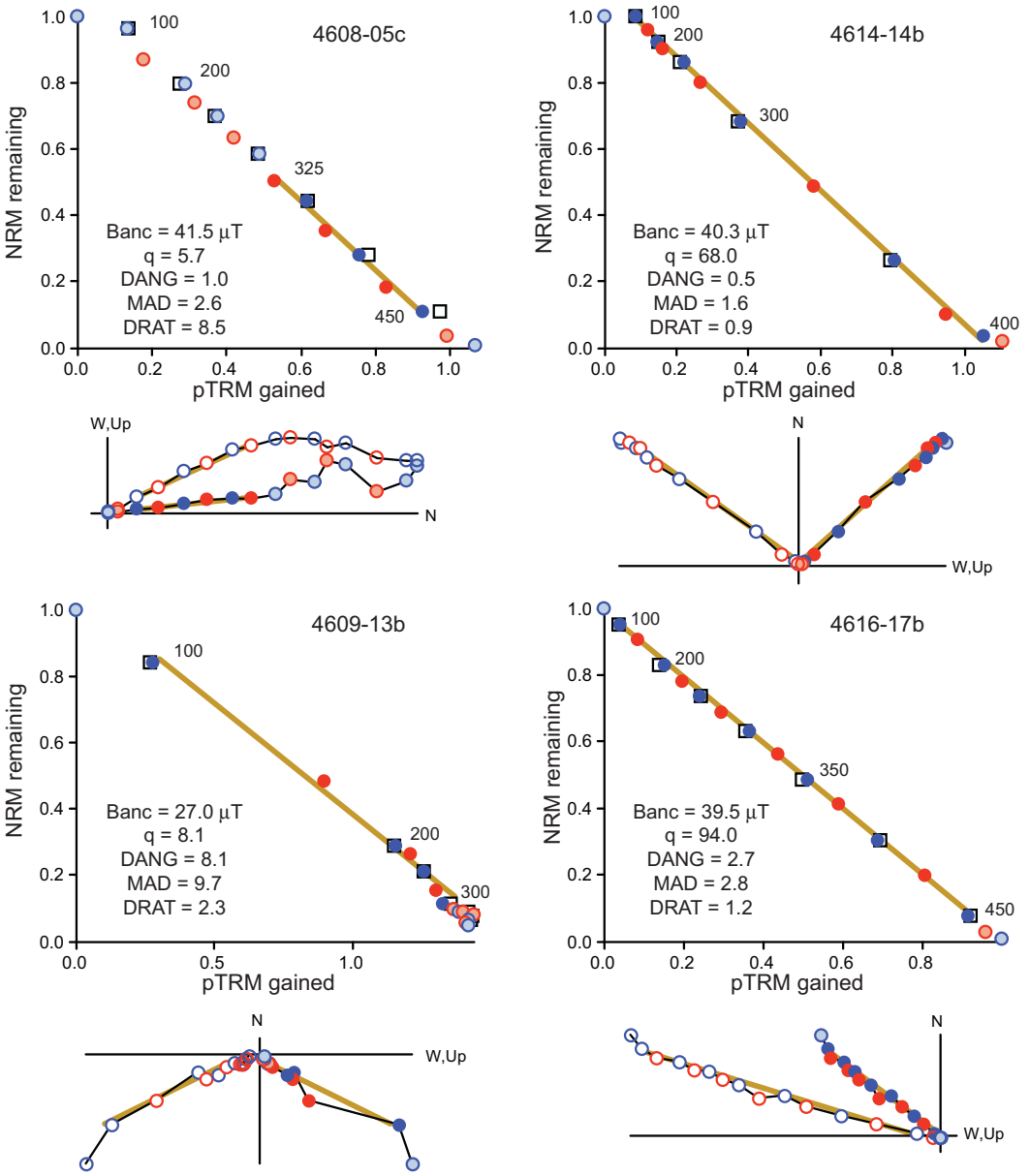

Figure 3. Representative paleointensity data spanning the range of accepted quality criteria. Top (Arai) plots show NRM lost versus pTRM gained, normalized to the NRM value. Selected temperatures (°C) are shown. Zero-field-first steps (ZI) blue, in-field-first (IZ) steps red. pTRM designated by squares. Bottom plots are vector endpoint diagrams representing the horizontal and vertical component of NRM as it is demagnetized (arbitrary coordinates). Banc = paleointensity interpretation based on the selected data points; q = quality factor [*Coe et al.*, 1978]; DANG = deviation angle [*Selkin et al.*, 2000]; MAD = maximum angular deviation [*Kirschvink*, 1980]; DRAT = difference ratio [*Selkin et al.*, 2000].

6c and 6d). Compared to the observed anomalies, the modeled anomalies are on average slightly more positive, with a mean (median) of 2.0 μT (1.5 μT) for the hummocky terrain (Figure 5c) and 1.5 μT (0.8 μT) for the faulted terrain (Figure 5d). As for the observed anomalies, the distributions are skewed positive, with skewness values of 0.7 and 1.1, for hummocky and faulted terrain, respectively. As expected, the largest anomalies are produced adjacent to large escarpments or on the north and south sides of large mounds or ridges. The discrepancy between measured and modeled anomaly distribution means could arise from a variety of sources, including the ±1 μT accuracy of the magnetometer; an insufficient vehicle correction; or insufficient spatial sampling of actual anomalies (for example, not sampling close enough to large scarps to capture the largest—and most positive—anomalies). Additionally, the model

Table 1. Sample Mean Paleointensity Results, Grouped by Flow Field

Sample	IGSN	Longitude	Latitude	B_{anc} (μT)	Standard Error (μT)	*N*
Calor						
4606-01	JMS000134	−91.9789	2.1110	37.0	1.3	7
4606-03	JMS000136	−91.9723	2.1096	30.9	1.2	5
4606-04	JMS000137	−91.9719	2.1068	39.5	0.5	4
4606-05	JMS000138	−91.9690	2.1079	33.3	0.4	5
4606-08	JMS000141	−91.9637	2.1057	37.6	0.5	5
4606-09	JMS000142	−91.9641	2.1084	41.5	0.6	5
4606-10	JMS000143	−91.9654	2.1071	33.3	0.5	5
4606-11	JMS000144	−91.9657	2.1067	33.3	0.5	4
4608-07	JMS000159	−91.9367	2.1056	37.0	0.6	5
4608-08	JMS000160	−91.9365	2.1039	35.0	1.1	4
4611-04	JMS000198	−91.9225	2.1047	37.9	0.7	5
4616-04	JMS000257	−91.9377	2.1013	35.6	1.7	1
4616-05	JMS000258	−91.9386	2.1023	34.9	1.8	4
4616-06	JMS000259	−91.9385	2.1028	37.3	0.5	4
4616-07	JMS000260	−91.9384	2.1036	39.3	1.1	5
4616-13	JMS000266	−91.9328	2.1052	42.5	1.3	8
4616-14	JMS000267	−91.9322	2.1057	42.2	1.8	4
4616-15	JMS000268	−91.9338	2.1061	40.6	0.8	5
4616-16	JMS000269	−91.9347	2.1069	36.5	1.4	7
4617-10	JMS000280	−91.9826	2.1081	25.3	3.3	2
Cobija						
4609-01	JMS000166	−91.9054	2.0944	38.9	0.4	1
4611-01	JMS000195	−91.9231	2.1114	41.5	1.3	8
4611-02	JMS000196	−91.9229	2.1092	39.8	1.6	5
4611-03	JMS000197	−91.9229	2.1092	37.4	0.7	4
4615-06	JMS000242	−91.9020	2.0928	40.6	1.4	4
4615-07	JMS000243	−91.9036	2.0926	45.7	1.0	6
4615-08	JMS000244	−91.9066	2.0944	42.5	1.7	5
4616-17	JMS000270	−91.9405	2.1134	39.2	0.4	4
Empanada						
4607-06	JMS000150	−91.9562	2.1110	34.9	1.3	7
4607-07	JMS000151	−91.9557	2.1082	37.9	0.8	6
4607-08	JMS000152	−91.9550	2.1047	38.1	0.8	5
4608-03	JMS000155	−91.9432	2.1040	34.1	0.8	4
4608-04	JMS000156	−91.9430	2.1050	38.8	1.9	4
4608-05	JMS000157	−91.9426	2.1061	39.9	1.0	9
4616-01	JMS000254	−91.9349	2.0985	43.1	1.5	2
4616-02	JMS000255	−91.9361	2.0999	38.9	1.0	4
4616-03	JMS000256	−91.9370	2.1007	37.7	0.6	4
4616-08	JMS000261	−91.9366	2.1023	35.6	1.4	3
4616-10	JMS000263	−91.9346	2.1032	38.1	0.7	4
Niños						
4608-06	JMS000158	−91.9410	2.1061	39.9	1.7	4
4608-11	JMS000163	−91.9287	2.1029	44.4	0.5	4
4609-02	JMS000167	−91.9047	2.0959	37.6	1.3	2
4609-03	JMS000168	−91.9042	2.0983	38.0	3.1	3
4609-04	JMS000169	−91.9045	2.0997	35.9	1.2	5
4609-06	JMS000171	−91.9068	2.1023	41.8	1.9	4
4609-07	JMS000172	−91.9084	2.1015	30.8	1.3	4
4609-08	JMS000173	−91.9113	2.1007	40.4	2.3	5
4609-09	JMS000174	−91.9124	2.1005	36.2	0.7	4
4609-13	JMS000178	−91.9222	2.1020	32.7	0.1	1
4611-05	JMS000199	−91.9219	2.1030	36.9	0.5	1
4611-06	JMS000200	−91.9271	2.1040	36.5	1.5	4
4611-08	JMS000202	−91.9284	2.1043	39.9	1.7	5
4614-05	JMS000226	−91.9021	2.0997	35.8	0.9	4
4614-06	JMS000227	−91.9012	2.0988	32.4	1.2	6
4614-09	JMS000230	−91.8952	2.0985	42.0	1.3	5
4614-14	JMS000235	−91.8998	2.0958	41.3	1.1	5
4615-12	JMS000248	−91.9108	2.1016	38.4	1.5	7
4615-15	JMS000251	−91.9095	2.1019	30.5	0.8	4

magnetization of 35 Am^{-1} could be too high on average (the magnetic source layer likely varies in thickness and magnetization), or there could be a long-wavelength regional anomaly not taken into account by the modeling.

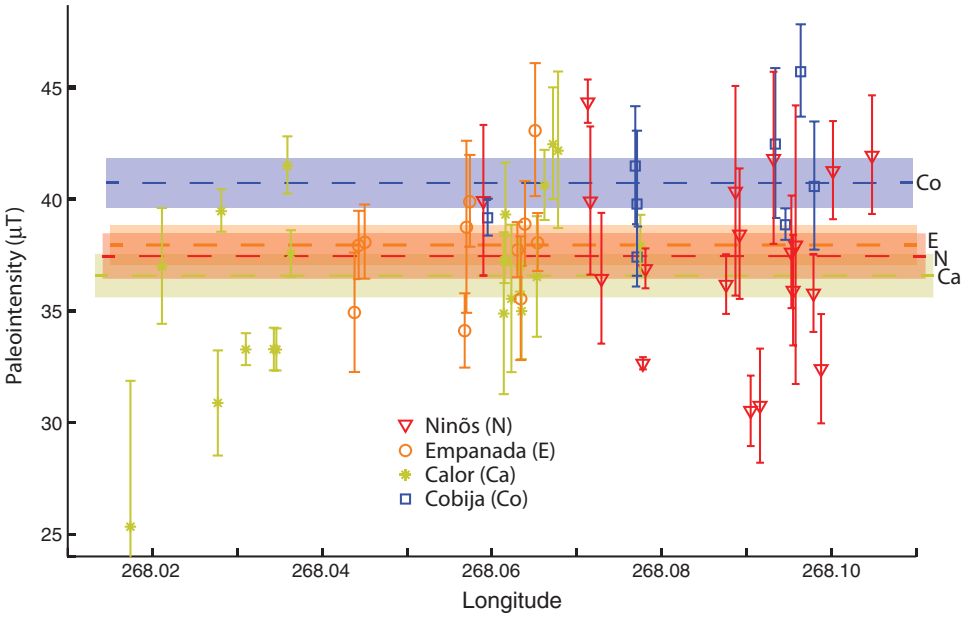

Figure 4. Paleointensity versus along-axis longitude, grouped by flow field. Sample-level error bars represent two standard errors about the mean. Horizontal dashed lines represent flow field means, and shaded horizontal boxes represent one standard error about flow field mean.

5. Discussion

5.1. Assigning Ages to the Flows

The amount of scatter in paleointensity values within the defined flow fields is substantial. If the scatter represents true variation in time of the core-derived field, the implication is that individual flow fields erupted over many decades or even hundreds of years. This interpretation is unlikely as it would also imply that the flow fields were being emplaced simultaneously from different magma sources in order to account for the distinct chemical composition of each field [*Colman et al.*, 2012]. A further implication would be the coexistence and tapping during eruptions of geochemically distinct magma chambers in very close proximity for hundreds of years. This interpretation also is inconsistent with the compiled durations and recurrence intervals for all known mid-ocean ridge eruptions, which are generally $<$1 year and 1–2 decades, respectively [*Rubin et al.*, 2012].

By contrast, both the measured and modeled local anomalies are sufficient to explain the observed within-flow scatter in paleointensity data. As noted above, the magnitude of the anomalies is likely correlated with the steepness and geometry of the topography and with the magnetization of the flows. Magnetization has been found to scale with iron content [*Anderson et al.*, 1975; *Gee and Kent*, 1998; *Vogt and De Boer*, 1976], but we find no significant correlation between flow-mean FeO [*Colman et al.*, 2012] and either anomaly amplitude or scatter in measured paleointensity values as measured by flow unit standard deviation.

However, we do find correlations between increased topographic relief and both of these variables. In general, pillow lavas tend to produce constructional edifices with greater relief, followed by lobate flows and then sheet flows. The larger topographic gradients associated with pillow mounds or ridges should generate larger anomalies. To test this, we calculated the mean and median anomaly amplitude (absolute value of anomaly) measured above pillow, lobate, and sheet flows. We find that anomaly amplitude decreases from pillow to lobate to sheet flow (Figure 7). The mean (median) anomaly amplitude measured over all pillow lavas is 3.4 μT (2.5 μT), while that over sheet flows is 2.0 μT (1.3 μT). For the HMS area alone, the mean (median) is 3.1 μT (2.3 μT) for pillows and

Table 2. Flow-Mean Paleointensity

Flow	Mean (μT)	Standard Error (μT)	N
Calor (Ca)	36.6	1.0	20
Cobija (Co)	40.7	1.1	8
Empanada (E)	38.0	0.9	11
Ninos (N)	37.5	1.0	19

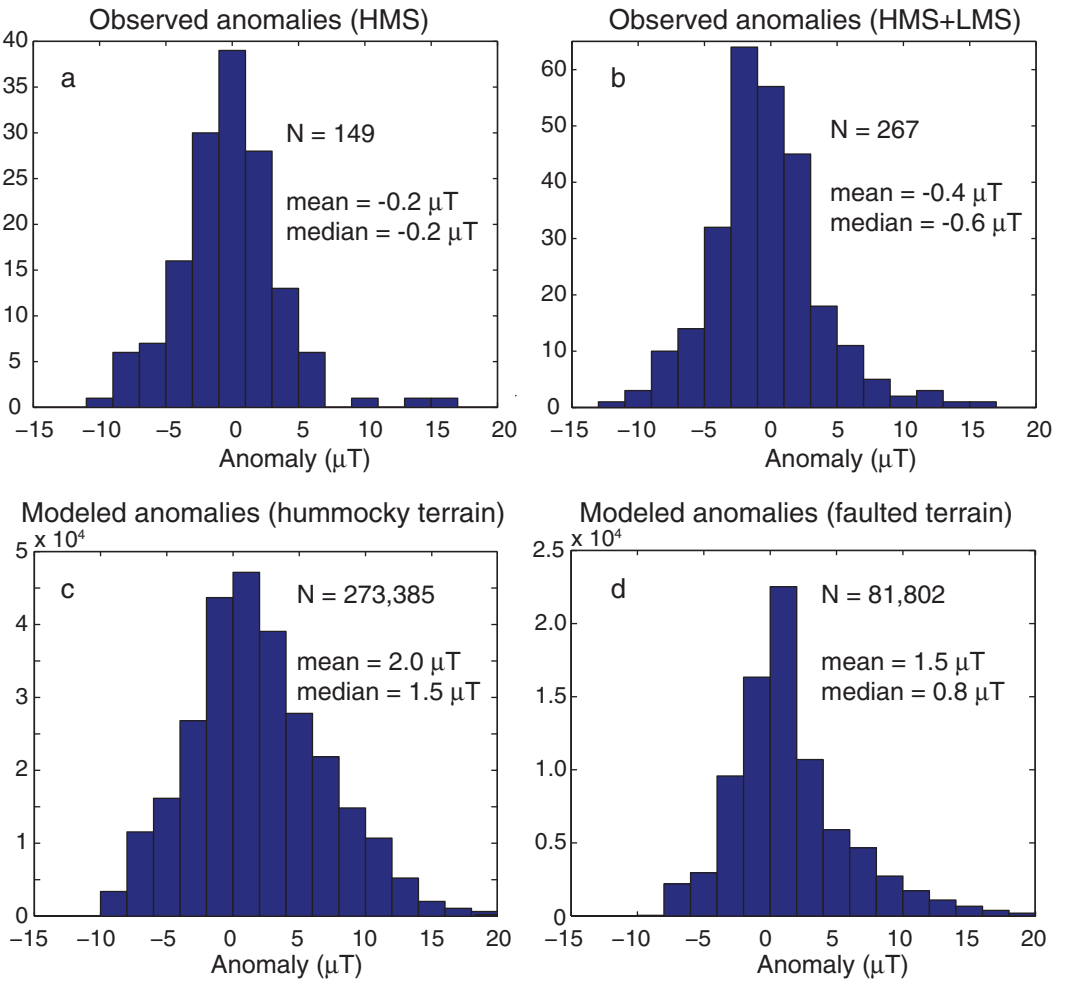

Figure 5. Histograms of observed and modeled magnetic anomaly distributions. Observed near-bottom anomalies (~3 m above bottom) at (a) high-magma-supply (HMS) study area only and (b) combined distribution for HMS and low-magma-supply (LMS) study area. Modeled anomalies at 10 m above bottom for (c) predominantly hummocky terrain (Figures 6a and 6b) and (d) predominantly faulted terrain (Figures 6c and 6d).

1.5 μT (1.0 μT) for sheets. In the HMS study area, the maximum anomaly amplitude decreases from 14.8 μT over pillows to only 6.1 μT over sheets.

Decreased anomaly amplitudes over flows with little relief suggests that improved flow-mean paleointensity estimates might be obtained by only sampling from lobates and/or sheets. However, this strategy assumes that similar magnitude anomalies were present prior to the emplacement of the currently sampled flows. To test for evidence of actual anomalies recorded by sampled flows, we additionally calculated flow-mean paleointensity for samples collected from pillow, lobate, and sheet flows. For all flows except Ninos, flow-mean paleointensity and standard deviation decrease from pillows to lobates to sheets. The number of sheet flows is small ($\leq$3) for all flow fields; grouping lobates and sheets together for better statistics gives a mean paleointensity that is 1.2–1.6 μT lower than the pillows mean. For Ninos, it is 0.6 μT higher. This suggests that the topographically induced anomalies may have a slight positive bias, the magnitude of which is in agreement with the modeling results. Excluding data from pillows, however, does not significantly change the overall interpretation and results in a very small number of samples for some flow fields that are dominated by pillow morphology. In the final analysis, we therefore include all samples, regardless of flow type.

In spite of the within-flow variability, the paleointensity results allow us to place some age constraints on the flows and suggest an episodicity in eruptive timing. First, the three youngest sampled flow fields are

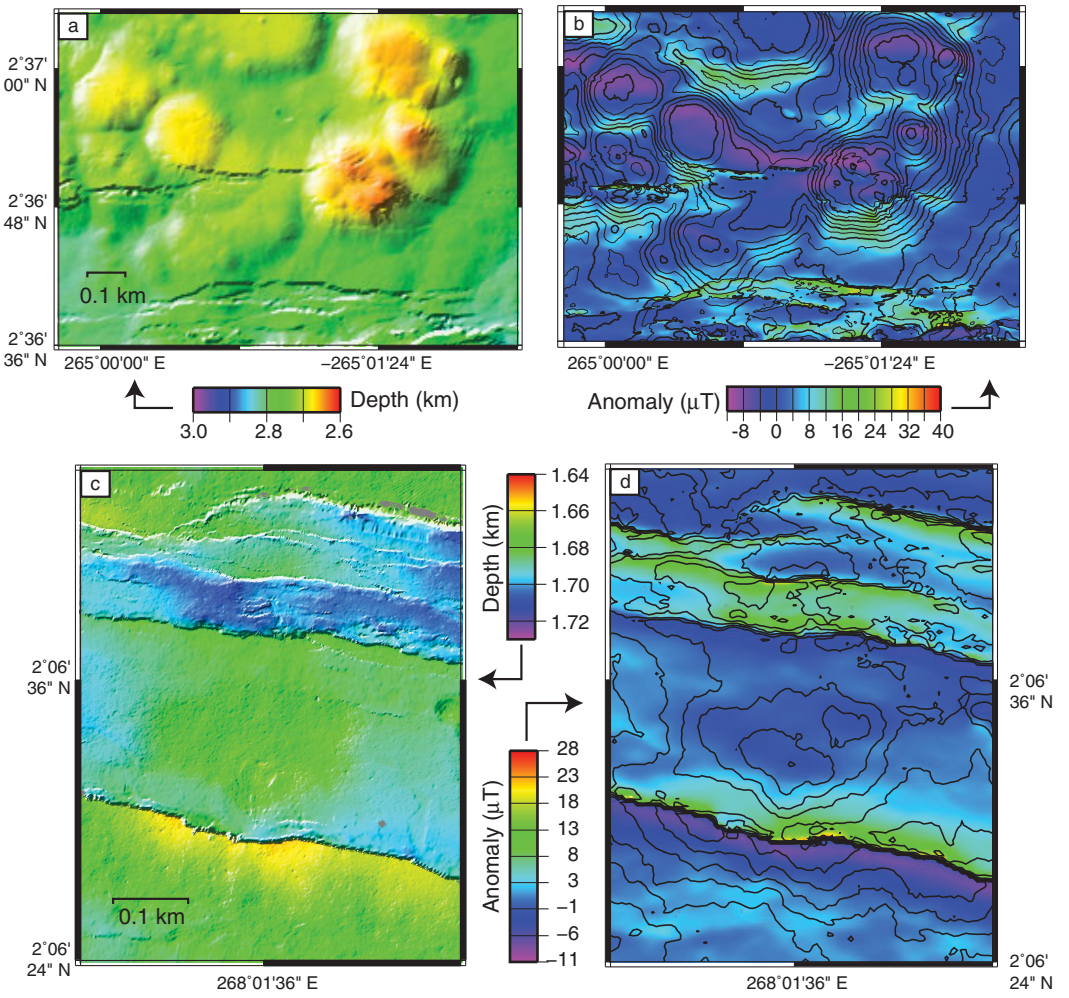

Figure 6. Modeled topographic-induced magnetic anomalies. Anomalies calculated at 10 m above bottom. (a) Bathymetry and (b) total field anomaly for predominantly hummocky terrain. (c) Bathymetry and (d) total field anomaly for predominantly faulted terrain.

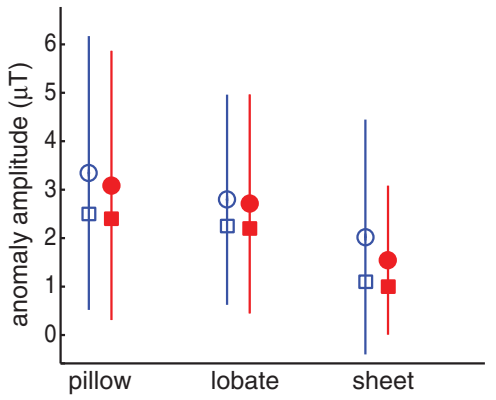

Figure 7. Anomaly amplitude measured above different flow morphologies. Anomaly amplitude is the absolute value of the total field anomaly. Blue, open symbols are HMS and LMS study areas combined. Red, closed symbols are HMS only. Circles are means, squares are medians, and error bars are ± one standard deviation.

indistinguishable in age based on paleointensity results, suggesting they were emplaced in relatively rapid succession. Second, the fourth flow has a significantly higher paleointensity, consistent with it being older. (Both results hold true even when we exclude pillow samples.) To step beyond relative age assignments, we compare the flow-mean paleointensity values with models of field behavior over the past several hundred years. In Figure 8, we show paleointensity variations based on both historical data (gufm model of *Jackson et al.* [2000]) and on

archeomagnetic, sedimentary, and volcanic data (CALs3k models of *Korte et al.* [2009]). Flow field (Table 2) means include all samples regardless of flow morphology. If we assume these means are accurate, then the three youngest flows were likely erupted in relatively close succession between 100 and 200 years ago, and the oldest flow is (very approximately) 400 years old. However, keeping in mind that flow field means might be biased slightly high (by 1–2 μT), the younger flows may be as young as ~50 years, and the older flow field has considerably more uncertainty in age, putting it at ~200–400 years old.

5.2. Eruptive Frequency and Episodicity

With or without a bias in paleointensity, the data are consistent with an episodic emplacement of the largest flow units: at least one relatively large flow emplaced ~400 years ago followed by a ~200–300 year period of relative quiescence, followed by the emplacement of three more relatively large flows. In this study area, there are at least two additional smaller flow fields in Figure 2 that were not sampled for paleointensity analyses and whose ages are interpreted as being intermediate between the three youngest flows and the oldest flow, based on observations of sediment cover and geological relationships. An additional two small flow fields on the central part of the ridge segment lie to the east of the region shown in Figure 2, and are younger than Cobija [*Colman et al.*, 2012]. The period of quiescence between emplacement of larger flows (when smaller flows were likely emplaced) is therefore not entirely amagmatic. However, without additional age constraints, we cannot say how the smaller flows are distributed within the quiescent interval. If we take these additional flows into account, there have been at least eight eruptive episodes (including Cobija) on the segment central region over the past 200–400 years, suggesting an average eruptive recurrence interval maximum of 25–50 years.

The episodic nature of eruptive activity and the scarcity of data make it difficult to compare eruptive behavior at different mid-ocean ridge locations using the new and literature data. One way such comparisons are typically made is to simplify the system by calculating an average eruption interval. Quantifying an average eruption interval using a limited time-slice while knowing activity has been episodic is challenging, so we briefly review existing points of comparison for both episodicity and average eruption frequencies at mid-ocean ridges.

As noted above (section 1), episodicity has been observed in several different mid-ocean ridge environments. At 17°30′S on the fast spreading East Pacific Rise (EPR), both paleointensity and ^{210}Pb-^{226}Ra ages suggest that five or six flows are distributed unevenly over the past ~400 years, with the youngest two or three less than 100 years old [*Bergmanis et al.*, 2007]. On the northern EPR, paleointensity data suggest a similar episodicity may extend to larger spatial scales and longer time periods; relatively small on-axis flows may recur with repose periods of tens to hundreds of years, while periods of extensive off-axis lava emplacement appear to be episodic on 10–20 kyr time scales [*Bowles et al.*, 2006]. At 45°N on the slow spreading Mid-Atlantic Ridge, *Searle et al.* [2010] find that construction of an axial volcanic ridge is likely to be episodic in nature, and paleointensity data constrain its age to be at least 1 ka, but <12 ka. For hot spot-influenced ridge segments (with relatively high magma supply for a given spreading rate), *Nooner and Chadwick* [2009] contrast subaerial Iceland with submarine Axial seamount. At Iceland, 10–

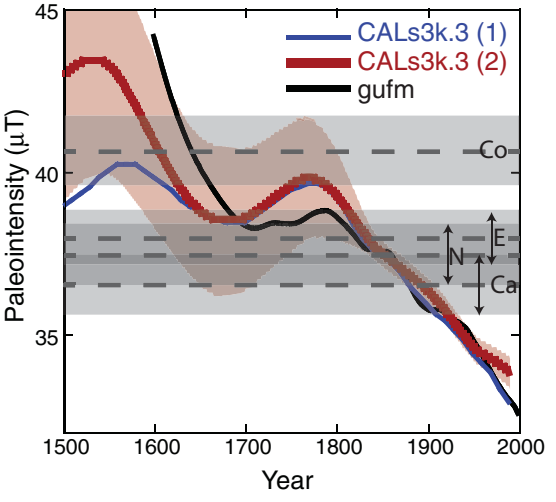

Figure 8. Models of paleointensity versus time evaluated at the study site. *gufm* model is based on historical data [*Jackson et al.*, 2000]. CALs3k.3 model [*Korte et al.*, 2009] is based on archeomagnetic, sedimentary and volcanic data. CALs3k.3(1) excludes less reliable data as determined by *Korte et al.* [2009], while CALs3k.3(2) includes all available data and shows calculated uncertainty bounds. Flow field mean paleointensity shown by horizontal dashed lines with ±1 standard error.

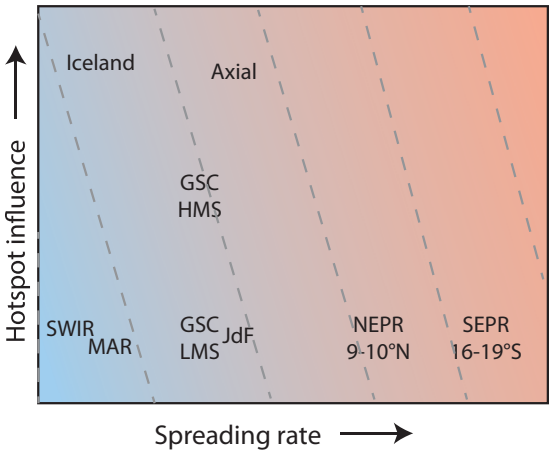

Figure 9. Schematic representation of magma supply as a function of spreading rate and proximitiy to hot spot. Color represents relative magma supply from low (blue) to high (red). Gray dashed lines represent lines of approximately equal magma supply. MAR = Mid-Atlantic Ridge (away from hot spot); SWIR = Southwest Indian Ridge; GSC-HMS(LMS) = Galapagos Spreading Center—high magma supply (low magma supply); JdF = Juan de Fuca Ridge (away from hot spot) NEPR, SEPR = northern or southern East Pacific Rise.

20 diking events (only a few of which are accompanied by eruptions) may be clustered within ~10 years, separated by 200–300 years. By contrast, at Axial seamount individual eruptions are spaced ~20 years apart. Subsequent work at Axial [*Clague et al*., 2013] is consistent with this observation, but additionally suggests that Axial has had at least two phases of more frequent eruptive activity lasting from 245 to 360 years, separated by a relatively quiescent phase of ~345 years.

The average eruptive interval maximum we find along the mapped 16 km central ridge segment region (25–50 year) is slightly less than an estimate of 72 years for the same location based on average extrusive layer thickness and median flow volume estimates [*Colman et al*., 2012] and calculated over 16 km ridge length. A similar estimate at our LMS study area is 360 years [*Colman et al*., 2012], and comparable estimates for other locations range from 9 to 43 years on the southern EPR [*Sinton et al*., 2002] to hundreds or thousands of years along the slow spreading Mid-Atlantic Ridge [*Perfit and Chadwick*, 1998]. At the summit of hot spot-influenced Axial seamount, the average recurrence interval calculated using ^{14}C dating of overlying sediments is 11–19 years for the most recent ~360 year interval of frequent eruptive activity [*Clague et al*., 2013]. Alternatively, considering only intracaldera flows over the past ~800 years, the average interval is 20–25 years. Historical recurrence intervals between two eruptions, while not representing a statistical average, provide additional points of comparison. Our HMS average interval is slightly longer than historical intervals of ~14 years on the fast spreading EPR at 9°50′N; ~12–13 years on the intermediate-spreading CoAxial segment of the Juan de Fuca Ridge; and ~13 years on Axial Seamount [*Rubin et al*., 2012].

In terms of average eruptive frequency, our HMS study site falls somewhere between that of the LMS site, also on the GSC, and hot spot-influenced Axial seamount or the non-hot spot-influenced parts of the north and south EPR. At the same time, the duration of the quiescent phase we find (200–300 years) is similar to that observed in Iceland, at Axial volcano, and possibly along the southern EPR.

When placing our study site in the context of global mid-ocean ridge behavior, it is helpful to consider that eruptive behavior is governed not just by spreading rate, but also by magma supply, which is influenced by hot spot proximity. As noted above (section 1), eruption frequency typically increases with spreading rate. It has also been recently demonstrated that independent of spreading rate, eruption frequency increases with magma supply [*Colman et al*., 2012], which we also see here. Both magma supply and average eruption frequency appear to increase from LMS to HMS to Axial seamount, although all three sites have a similar spreading rate. Figure 9 illustrates this schematically and shows why our HMS study site on the intermediate-spreading GSC may share some commonalities with both Iceland (low spreading rate and strong hot spot influence) and with the north and south EPR (fast spreading rate but not hot spot influenced). This is, of course, an oversimplification. Eruptive episodicity and frequency are linked to a complicated set of codependent variables including spreading rate; rate of magma supply; depth and persistence of the magma chamber or melt lens; and thickness and strength of the lithosphere. Teasing out exact relationships will require a considerable increase in available data (numbers of sites and eruptions), emphasizing the importance of obtaining additional eruption chronologies like the one presented here.

6. Conclusions

A large number of paleointensity analyses have been carried out on samples collected from four mapped flow fields from the intermediate-spreading Galapagos Spreading Center, with the goal of placing temporal constraints on volcanic eruptions. Three relatively large, young flow fields are indistinguishable in age and were emplaced in relatively rapid succession sometime in the past 100–200 years. The oldest sampled flow field is significantly older, roughly ~400 years old. A possible bias in the paleointensity data allows for younger ages of as little as ~50 years old for the younger three flows and 200–400 years old for the oldest flow. There is an implied episodicity in the emplacement of these four largest flows, with a 200–300 year period of relative quiescence between emplacement of the oldest flow field and the three younger flow fields. Taking into account all eight mapped flow fields in the mapped central ridge segment study area, we find an average eruptive recurrence interval maximum of 25–50 years.

This study represents an important addition to the small number of absolute eruption chronologies that exist for mid-ocean ridges. The episodicity inherent in mid-ocean ridge eruptive behavior makes it difficult to quantify and to make comparisons with controlling variables such as spreading rate and magma supply. Additional data such as that presented here will be critical in efforts to fully describe and understand mid-ocean ridge eruptive behavior.

As expected, the paleointensity dating method has some limitations in this region of high near-bottom magnetic anomalies. Scatter in within-flow field paleointensity values can be explained by topographically induced magnetic anomalies. Measured on-bottom anomalies range from −9.6 to 14.8 μT with a mean of −0.2 μT, and modeled anomalies have a similar distribution but with a slightly higher mean (+1.5 to +2.0 μT). Flow morphology correlates with anomaly amplitude, with the highest amplitudes found over relatively high-relief pillow flows. Flow field mean paleointensity and standard deviation also correlate with flow morphology in three out of four flow fields. Higher paleointensity and higher scatter are observed in pillow flows, suggesting that paleointensity means may be biased high by 1–2 μT, which is in agreement with results from modeled anomalies.

Acknowledgments

This work was supported by National Science Foundation grants OCE-0850052 to J.A.B.; OCE-0849813 to J.M.S. and K.H.R.; and OCE-0849711 to S.M.W. Many thanks go to Aslam Ab Fatah, Lindsay Ellingson, and Kelsi Ustipak for carrying out many of the paleomagnetic measurements. We are grateful to the *Alvin*, *Sentry*, and *TowCam* teams and to the crew of the R/V *Atlantis* cruise AT15-63 for all their at-sea assistance. Thanks to Jeff Gee for software used to plot paleointensity data. All paleomagnetic work was carried out at the Institute for Rock Magnetism (IRM) at the University of Minnesota. The IRM is supported by the Instrumentation and Facilities Program of the National Science Foundation, Earth Science Division, and by the University of Minnesota. Samples used in this research are registered with unique identifiers (IGSN) through geosamples.org. All paleomagnetic data presented in this paper are available from the Magnetics Information Consortium (MagIC) database (earthref.org/MAGIC/). Other data are available by e-mailing J. A. Bowles. Thanks to Yongjae Yu, one anonymous reviewer, and editor Thorsten Becker who provided comments that improved the manuscript.

References

Anderson, R. N., D. A. Clague, K. D. Klitgord, M. Marshall, and R. K. Nishimori (1975), Magnetic and petrologic variations along the Galapagos spreading center and their relation to the Galapagos melting anomaly, *Geol. Soc. Am. Bull.*, *86*, 683–694.

Bergmanis, E. C., J. Sinton, and K. H. Rubin (2007), Recent eruptive history and magma reservoir dynamics on the southern East Pacific Rise at 17 30′ S, *Geochem. Geophys. Geosyst.*, *8*, Q12O06, doi:10.1029/2007GC001742.

Blakely, R. J. (1996), *Potential Theory in Gravity and Magnetic Applications*, 464 pp., Cambridge Univ. Press, New York.

Bowles, J., J. Gee, D. V. Kent, E. Bergmanis, and J. M. Sinton (2005), Cooling rate effects on paleointensity estimates in submarine basaltic glass and implications for dating young flows, *Geochem. Geophys. Geosyst.*, *6*, Q07002, doi:10.1029/2004GC000900.

Bowles, J., J. S. Gee, D. V. Kent, M. R. Perfit, S. A. Soule, and D. J. Fornari (2006), Paleointensity applications to timing and extent of eruptive activity, 9°-10°N East Pacific Rise, *Geochem. Geophys. Geosyst.*, *7*, Q06006, doi:10.1029/2005GC001141.

Bowles, J. A., J. S. Gee, K. Burgess, and R. F. Cooper (2011), Timing of magnetite formation in basaltic glass: Insights from synthetic analogs and relevance for geomagnetic paleointensity analyses, *Geochem. Geophys. Geosyst.*, *12*, Q02001, doi:10.1029/2010GC003404.

Carlut, J., and D. V. Kent (2000), Paleointensity record in zero-age submarine basalt glasses: Testing a new dating technique for recent MORBs, *Earth Planet. Sci. Lett.*, *183*, 389–401.

Carlut, J., M. H. Cormier, D. V. Kent, K. E. Donnelly, and C. H. Langmuir (2004), Timing of volcanism along the northern East Pacific Rise based on paleointensity experiments on basaltic glasses, *J. Geophys. Res.*, *109*, B04104, doi:10.1029/2003JB002672.

Clague, D. A., et al. (2013), Geologic history of the summit of Axial Seamount, Juan de Fuca Ridge, *Geochem. Geophys. Geosyst.*, *14*, 4403–4443, doi:10.1002/ggge.20240.

Coe, R. S. (1967), The determination of paleo-intensities of the earth's magnetic field with emphasis on mechanisms which could cause non-ideal behavior in Thellier's method, *J. Geomagn. Geoelectr.*, *19*, 157–179.

Coe, R. S., S. Gromme, and E. A. Mankinen (1978), Geomagnetic paleointensities from radiocarbon-dated lava flows on Hawaii and the question of the Pacific nondipole low, *J. Geophys. Res.*, *83*, 1740–1756.

Colman, A., et al. (2012), Effects of variable magma supply on mid-ocean ridge eruptions: Constraints from mapped lava flow fields along the Galápagos Spreading Center, *Geochem. Geophys. Geosyst.*, *13*, Q08014, doi:10.1029/2012GC004163.

Cormier, M.-H., W. B. F. Ryan, A. K. Shah, J. Wen, A. M. Bradley, and D. R. Yoerger (2003), Waxing and waning volcanism along the East Pacific Rise on a millennium time scale, *Geology*, *31*, 633–636.

Day, R., M. Fuller, and V. A. Schmidt (1977), Hysteresis properties of titanomagnetites: Grain-size and compositional dependence, *Phys. Earth Planet. Inter.*, *13*, 260–267.

Dreyer, B. M., D. A. Clague, and J. B. Gill (2013), Petrological variability of recent magmatism at Axial Seamount summit, Juan de Fuca Ridge, *Geochem. Geophys. Geosyst.*, *14*, 4306–4333, doi:10.1002/ggge.20239.

Dunlop, D. J. (2002), Theory and application of the Day plot (Mrs/Ms versus Hcr/Hc): 1. Theoretical curves and tests using titanomagnetite data, *J. Geophys. Res.*, *107*(B3), doi:10.1029/2001JB000486.

Fornari, D. J., R. M. Haymon, M. R. Perfit, T. K. P. Gregg, and M. H. Edwards (1998), Axial summit trough of the East Pacific Rise 9°–10°N: Geological characteristics and evolution of the axial zone on fast spreading mid-ocean ridges, *J. Geophys. Res.*, *103*, 9827–9855.

Fornari, D. J., et al. (2012), The East Pacific Rise between 9°N and 10°N: Twenty-five years of integrated, multidisciplinary oceanic spreading center studies, *Oceanography*, *25*, 18–43.

Gee, J., and D. V. Kent (1998), Magnetic telechemistry and magmatic segmentation on the Southern East Pacific Rise, *Earth Planet. Sci. Lett.*, *164*, 379–385.
Gudmundsson, A. (2000), Dynamics of volcanic systems in Iceland: Example of tectonism and volcanism at juxtaposed hot spot and mid-ocean ridge systems, *Ann. Rev. Earth Planet. Sci.*, *28*, 107–140.
Ito, G., and M. D. Behn (2008), Magmatic and tectonic extension at mid-ocean ridges: 2. Origin of axial morphology, *Geochem. Geophys. Geosyst.*, *9*, Q09O12, doi:10.1029/2008GC001970.
Jackson, A., A. R. T. Jonkers, and M. R. Walker (2000), Four centuries of geomagnetic secular variation from historical records, *Philos. Trans. R. Soc. London A*, *358*, 957–990.
Jackson, M., and P. Solheid (2010), On the quantitative analysis and evaluation of magnetic hysteresis data, *Geochem. Geophys. Geosyst.*, *11*, Q04Z15, doi:10.1029/2009GC002932.
Kappel, E. S., and W. B. F. Ryan (1986), Volcanic episodicity and a non-steady state rift valley along Northeast Pacific spreading centers: Evidence from Sea MARC I, *J. Geophys. Res.*, *91*, 13,925–13,940.
Kirschvink, J. L. (1980), The least-squares line and plane and the analysis of palaeomagnetic data, *Geophys. J. R. Astron. Soc.*, *62*, 699–718.
Korte, M., F. Donadini, and C. G. Constable (2009), Geomagnetic field for 0–3 ka: 2. A new series of time-varying global models, *Geochem. Geophys. Geosyst.*, *10*, Q06008, doi:10.1029/2008GC002297.
McClinton, T., S. M. White, A. Colman, and J. M. Sinton (2013), Reconstructing lava flow emplacement processes at the hotspot-affected Galápagos spreading center, 95°W and 92°W, *Geochem. Geophys. Geosyst.*, *14*, 2731–2756, doi:10.1002/ggge.20157.
Nooner, S. L., and W. W. Chadwick Jr. (2009), Volcanic inflation measured in the caldera of Axial Seamount: Implications for magma supply and future eruptions, *Geochem. Geophys. Geosyst.*, *10*, Q02002, doi:10.1029/2008GC002315.
Perfit, M. R., and W. W. Chadwick (1998), Magmatism at mid-ocean ridges: Constraints from volcanological and geochemical investigations, in *Faulting and Magmatism at Mid-Ocean Ridges*, vol. 106, edited by R. W. Buck et al., pp. 59–115, AGU, Washington, D. C.
Rubin, K., J. D. Macdougall, and M. R. Perfit (1994), ^{210}Po-^{210}Pb dating of recent volcanic eruptions on the sea floor, *Nature*, *368*, 841–844.
Rubin, K., I. van der Zander, M. C. Smith, and E. Bergmanis (2005), Minimum speed limit for ocean ridge magmatism from ^{210}Pb-^{226}Ra-^{230}Th disequilibria, *Nature*, *437*, 534–538.
Rubin, K. H., S. A. Soule, W. W. Chadwick, D. J. Fornari, D. A. Clague, R. W. Embley, E. T. Baker, M. R. Perfit, D. W. Caress, and R. P. Dziak (2012), Volcanic eruptions in the deep sea, *Oceanography*, *25*, 142–157.
Ryan, W. B. F., et al. (2009), Global multi-resolution topography synthesis, *Geochem. Geophys. Geosyst.*, *10*, Q03014, doi:10.1029/2008GC002332.
Searle, R. C., B. J. Murton, K. Achenbach, T. LeBas, M. Tivey, I. Yeo, M. H. Cormier, J. Carlut, P. Ferreira, and C. Mallows (2010), Structure and development of an axial volcanic ridge: Mid-Atlantic Ridge, 45°N, *Earth Planet. Sci. Lett.*, *299*, 228–241.
Selkin, P., and L. Tauxe (2000), Long-term variations in palaeointensity, *Philos. Trans. R. Soc. London A*, *358*, 1065–1088.
Sims, K. W. W., S. R. Hart, M. K. Reagan, J. Blusztajn, H. Staudigel, R. A. Sohn, G. D. Layne, L. A. Ball, and J. Andrews (2008), ^{238}U-^{230}Th-^{226}Ra-^{210}Pb-^{210}Po, ^{232}Th-^{228}Ra, and ^{235}U-^{231}Pa constraints on the ages and petrogenesis of Vailulu'u and Malumalu Lavas, Samoa, *Geochem. Geophys. Geosyst.*, *9*, Q04003, doi:10.1029/2007GC001651.
Sinton, J., E. Bergmanis, K. Rubin, R. Batiza, T. K. P. Gregg, K. Gronvold, K. C. Macdonald, and S. M. White (2002), Volcanic eruptions on mid-ocean ridges: New evidence from the superfast spreading East Pacific Rise, 17°–19°S, *J. Geophys. Res.*, *107*(B6), doi:10.1029/2000JB000090.
Sinton, J., R. Detrick, J. P. Canales, G. Ito, and M. Behn (2003), Morphology and segmentation of the western Galápagos Spreading Center, 90.5°–98°W: Plume-ridge interaction at an intermediate spreading ridge, *Geochem. Geophys. Geosyst.*, *4*(12), 8515, doi:10.1029/2003GC000609.
Sinton, J., K. Gronvold, and K. Saemundsson (2005), Postglacial eruptive history of the Western Volcanic Zone, Iceland, *Geochem. Geophys. Geosyst.*, *6*, Q12009, doi:10.1029/2005GC001021.
Tanguy, J.-C., and M. Le Goff (2004), Distortion of the geomagnetic field in volcanic terrains: An experimental study of the Mount Etna stratovolcano, *Phys. Earth Planet. Inter.*, *141*, 59–70.
Tauxe, L., and H. Staudigel (2004), Strength of the geomagnetic field in the Cretaceous Normal Superchron: New data from submarine basaltic glass of the Troodos Ophiolite, *Geochem. Geophys. Geosyst.*, *5*, Q02H06, doi:10.1029/2003GC000635.
Thellier, E., and O. Thellier (1959), Sur l'intensité du champ magnétique terrestre dans le passé historique et géologique, *Ann. Geophys.*, *15*, 285–378.
Tivey, M. A., P. A. Rona, and H. Schouten (1993), Reduced crustal magnetization beneath the active sulfide mound, TAG hydrothermal field, Mid-Atlantic Ridge at 26 N, *Earth Planet. Sci. Lett.*, *115*, 101–115.
Valet, J.-P., and V. Soler (1999), Magnetic anomalies of lava fields in the Canary islands. Possible consequences for paleomagnetic records, *Phys. Earth Planet. Inter.*, *115*, 109–118.
Vogt, P. R., and J. De Boer (1976), Morphology, magnetic anomalies and basalt magnetization at the ends of the Galapagos high-amplitude zone, *Earth Planet. Sci. Lett.*, *33*, 145–163.